Mechanisms of void nucleation on neat and Glass Syntactic PolyPropylene using in situ synchrotron radiation tomography

Theophile Hourdou, Cristian Ovalle, Sebastien Blassiau, Alain Thionnet, Lucien Laiarinandrasana

▶ **To cite this version:**

Theophile Hourdou, Cristian Ovalle, Sebastien Blassiau, Alain Thionnet, Lucien Laiarinandrasana. Mechanisms of void nucleation on neat and Glass Syntactic PolyPropylene using in situ synchrotron radiation tomography. Composites Part B: Engineering, 2024, 284, 10.1016/j.compositesb.2024.111696 . hal-04943282

HAL Id: hal-04943282
https://hal.science/hal-04943282v1

Submitted on 12 Feb 2025

HAL is a multi-disciplinary open access archive for the deposit and dissemination of scientific research documents, whether they are published or not. The documents may come from teaching and research institutions in France or abroad, or from public or private research centers.

L'archive ouverte pluridisciplinaire **HAL**, est destinée au dépôt et à la diffusion de documents scientifiques de niveau recherche, publiés ou non, émanant des établissements d'enseignement et de recherche français ou étrangers, des laboratoires publics ou privés.

Distributed under a Creative Commons Attribution 4.0 International License

Composites Part B 284 (2024) 111696

Contents lists available at ScienceDirect

Composites Part B

journal homepage: www.elsevier.com/locate/composites

Mechanisms of void nucleation on neat and Glass Syntactic PolyPropylene using *in situ* synchrotron radiation tomography

Theophile Hourdou [a], Cristian Ovalle [a,*], Sebastien Blassiau [b], Alain Thionnet [a,c], Lucien Laiarinandrasana [a]

[a] Mines Paris, PSL University, Centre for Material Sciences (CMAT), CNRS UMR 7633, BP 87 91003, Evry, France
[b] SAIPEM S.A., Subsea Engineering (SUB) Department, 8 avenue de Lunca - Montigny le Bretonneux, 78884 Saint Quentin en Yvelines, France
[c] Université de Bourgogne, Mirande, Dpt. IEM, BP 47870, Dijon, France

ARTICLE INFO

Keywords:
Syntactic foam
GSPP
in situ microtomography
Void nucleation

ABSTRACT

The mechanisms of void nucleation of a hollow glass syntactic foam during tensile loading were studied in depth. Flat-notched geometries, cut-out from neat and Glass Syntactic PolyPropylene (GSPP), were investigated by *in situ* microtomography. Notched specimens with two notch root radii, 4 mm and 0.15 mm named respectively N_4 and $N_{0.15}$, to set initial triaxial stress state in the minimum cross section, were observed. Tomographic data sets, with a resolution of 1.3 μm, from stepwise tensile loading, at the SOLEIL synchrotron radiation facilities, were retrieved from the notched zone. In addition, they allowed gathering both the width and thickness evolution in the minimum cross section, and the notch opening displacement during the tests.

In line with literature, neat PolyPropylene (PP) showed crazes concentration at the specimen core in N_4 specimen, whereas, in $N_{0.15}$ specimen, they were located at the notch root. In isolated Hollow Glass Microspheres (HGM), mechanisms of crazing and debonding were correspondingly highlighted in the PP matrix and at the poles of HGM. Finally, in GSPP, decohesion follows the same trend as in neat PP, *i.e.* at the specimen core and near the notch, respectively in N_4 and in $N_{0.15}$ geometry. Scenarios of void nucleation and propagation were outlined. The initiation of the brittle crack in the GSPP is mainly due to the matrix-HGM decohesion followed by the coalescence of near neighbouring caps.

1. Introduction

Syntactic foams[1] are lightweight polymer composites widely employed in petrochemical industries, sports, aerospace, and the subsea sectors due to their excellent mechanical properties and processability [2–5]. In a marine environment, the high specific strength can be beneficial due to the buoyancy achieved by their lightweight structure [6,7]. In addition, since the new legislation on carbon neutrality focuses on low carbon emissions, lightweight syntactic foams can be very advantageous for fuel-efficient transport, resulting in a reduction in carbon emissions. However, the main reason is still the relatively low thermal conductivity of the matrix material. Indeed, the purpose of wet insulation is to provide thermal insulation, and syntactic foams provide better thermal efficiency.

The effective mechanical properties of syntactic foams (SF) can be tailored by selecting an appropriate combination of matrix material and fillers. Among different type of hollow micro-particle fillers, *e.g.* hollow glass micro-spheres (HGMs), carbon and polymer microspheres, HGMs possess unique characteristics: Low density, low dielectric constant, outstanding thermal insulation and sound insulation [8]. The mechanical response of hollow glass-filled syntactic foams (HGSF) have been investigated thoroughly under compression [5,9–12], tension [10,12–14], and flexural loading [10,15]. Furthermore, using X-ray microtomography HGSF has been studied by *in situ* testing.

In [16], X-ray microtomography was used to qualitatively and quantitatively study the response of HGSF with different polymer resins during stepwise confined compression testing. The results have shown a homogeneous distribution of the damage features, affecting mainly the larger spheres, in the compliant resins (PolyPropylene PP and PolyUrethane PU) whereas, in the stiff one (epoxy), damage was localised in bands. The study was extended [17] to highlight the collapse of weaker microspheres and the swelling of the matrix during hydrostatic compression. Both investigations focused on bulk mechanical properties and the associated failure mechanism at quasi-static strain

* Corresponding author.
E-mail address: cristian.ovalle_rodas@minesparis.psl.eu (C. Ovalle).

[1] The foam is *syntactic* if it is made by mixing microballoons, ceramic spheres, or other lightweight aggregate, with a resin system [1].

https://doi.org/10.1016/j.compositesb.2024.111696
Received 5 March 2024; Received in revised form 17 June 2024; Accepted 2 July 2024
Available online 5 July 2024
1359-8368/© 2024 The Author(s). Published by Elsevier Ltd. This is an open access article under the CC BY license (http://creativecommons.org/licenses/by/4.0/).

rates. Conversely, in [18], the dynamic response of a HGSF with an epoxy matrix was investigated. In line with observations on foams deformed quasi-statically, the observations revealed that the failure process is dominated by the crushing of HGMs and the cracking of the resin. However, the mechanism of failure in the foam is significantly affected by the strain rate. More recently [19], digital volume correlation (DVC) during *in situ* compression revealed that both the initiation and propagation of HGMs collapse depended on the local clustering, leading to the formation of pseudo-crush bands in the composite — silicone elastomer HGSF. In [20], the study was broaden to highlight the particle clustering effects: The prevailing mechanism transitioned from dispersed to clustered HGMs collapse at low and at high volume fraction, respectively. However, no experimental data about the mechanisms of failure during *in situ* tensile loading are found in literature.

The mechanisms of failure during tensile loading have been deduced from the study of fracture surfaces, at the scale of laboratory specimens. The tensile fracture mechanism were related to particle–matrix debonding and matrix resin fracture in [12]. Furthermore, the tensile–compressive moduli difference was associated to debonding — during compression, debonding does not play an important role because the matrix is compressed on the particle and separation occurs only in a small region in the load transverse-direction. Debonding, caused by the complex stress state around the particle–matrix interface, was also evoked by [10]. In addition, brittle fracture was linked with the rough surface of the resin. In aforementioned observations, as well as in [13], a large number of surviving particles after the tensile test was noticed. Therefore, fracture surfaces brings insight about the kinetics of the failure mechanisms, but *a posteriori*.

In this study, the particle–matrix interaction and failure mechanisms of a HGSF during tensile loading was investigated. Flat-notched geometries were cut-out from neat and Glass Syntactic PolyPropylene (GSPP) extruded moulded plates. Notched specimens with two notch root radii, 4 mm and 0.15 mm named respectively N_4 and $N_{0.15}$, to set initial triaxial stress state in the minimum cross section, were used. Tensile tests and *in situ* tensile tests were respectively carried-out at the laboratory and at the SOLEIL synchrotron radiation facilities. Tomographic data sets, with a resolution of 1.3 μm, from stepwise tensile loading were retrieved from the notched zone. The tomographic data set allowed gathering both the width and thickness evolution in the minimum cross section, and the notch opening displacement (nod) during the tests. A qualitative study of the microstructure evolution in the net cross section during deformation in the following order is proposed: Neat PolyPropylene (resin), isolated Hollow Glass Microspheres (hollow filler), and Glass Syntactic PolyPropylene (syntactic foam).

This paper is organised as follows. The material under study and the specimen preparation are detailed in Section 2. In addition, the testing methods – tensile and *in situ* tests – and the tomographic data sets are commented. In Section 3, the results are discussed using an *inductive* framework, *i.e.* from the observations of the matrix resin, through the study of an isolated particle to the composite material. The paper is closed with the concluding remarks.

2. Materials and methods

2.1. Materials and microstructure

The materials under study are a PolyPropylene (PP), from outer layer of thermal insulation coating, and a Syntactic Glass PolyPropylene composite (GSPP). The materials were supplied as extruded plates by SAIPEM S.A.

The PP has a glass transition temperature $T_g = 0\,°C$. The main characteristics of PP are summarised in Table 1.

Hollow Glass Microspheres (HGM), supplied by 3M Corporation, were stirred continuously but slowly to ensure uniform dispersion. In order to check the HGM distribution within the PP matrix, a fracture surface of the GSPP was examined by Scanning Electron Microscopy (SEM).

Table 1
Physical properties of PolyPropylene (PP).

Density (base resin)	kg/m^3	910
Melt flow rate	g/10 min	4
Melt volume flow rate	cm^3/10 min	5.4

Table 2
Physical properties of Syntactic Glass PolyPropylene composite (GSPP).

Density of compound	g/cm^3	0.67
Volume fraction of spheres	%	30

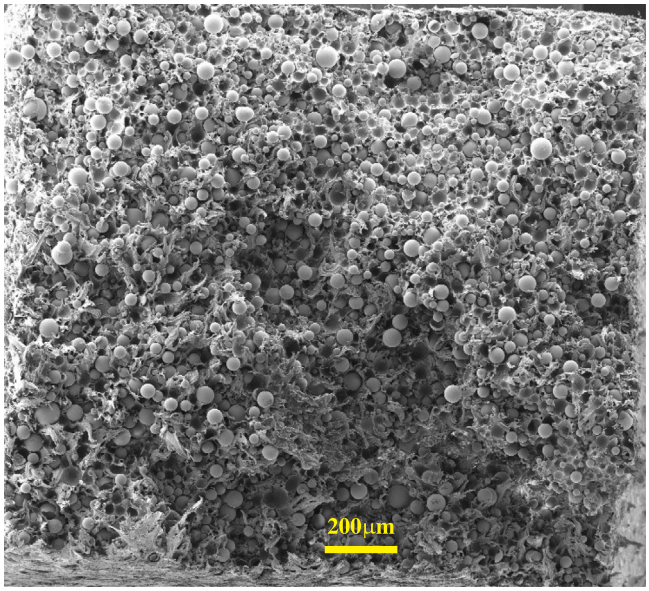

Fig. 1. SEM observation of the fracture surface of the GSPP showing HGM distribution.

The SEM fractography in Fig. 1 revealed a homogeneous distribution of the HGM, with a 30 vol% concentration in the PP matrix. Moreover, by using several micrographs together with granulometry analysis, an average diameter of about 15 μm was estimated. The decohesion between these HGMs and the PP matrix should act as the mechanisms of nucleation of void within the matrix.

GSPP was obtained by extrusion moulding. Table 2 presents the main nominal properties of the GSPP material used here (PolyPropylene, PP, matrix with Hollow Glass Microspheres, HGM).

2.2. Specimens

Flat notched specimens, H2 geometry [21] with 75 mm length, were cut-out from extruded moulded plates with 2 mm thickness. Specimens longitudinal axis corresponds to the extrusion direction. Two specimen geometries were considered, with machined double or single notches as illustrated in Fig. 2.

The double-notched specimens (Fig. 2(a)) were used to study the macroscopic mechanical response of the material using the laboratory facilities. Notched specimens with two notch root radii, 4 mm and 0.15 mm named respectively N_4 and $N_{0.15}$, to set initial triaxial stress state in the minimum cross section, were used [22]. The double notches, distant by 9.7 mm, were machined at mid-length. During the test, just one notch is expected to fail, giving two fracture surfaces to be analysed by SEM (see Fig. 1). The non-broken notch could then be

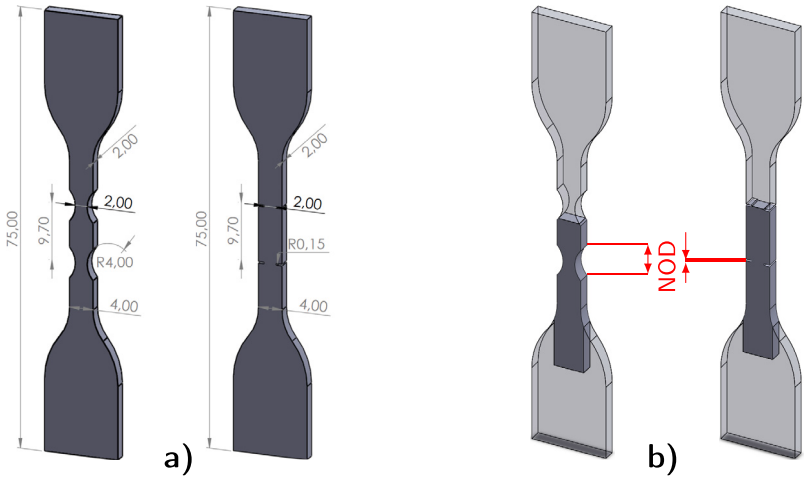

Fig. 2. Sketches of notched tensile specimens (N_ρ), ρ respectively, 4 mm and 0.15 mm, being the notch root radius: (a) characteristic lengths in mm of double notched specimens; (b) Reduced single notched specimens, in dark grey, for *in-situ* tests for tomography technique. (For interpretation of the references to colour in this figure legend, the reader is referred to the web version of this article.)

examined by *ex-situ* tomography. In this latter case, the microstructure is supposed to be at the state prior to the failure.

Reduced single-notched geometries were cut-out from double-notched ones at mid-length, due to the space limitation in the *in situ* tomography tensile rig. *In situ* tests directly allow the evolution of the microstructure to be followed during the test, there is therefore no need for a second notch.

The Notch Opening Displacement (NOD), which is thoroughly used in this work, is indicated in Fig. 2b. Following the definition of the crack mouth opening displacement in the Fracture Mechanics specimens, it was considered here as the distance between the two notch sides at the surface. During loading, this opening displacement, which constitutes a local measurement, continuously increases.

In this study, by opposition to cylindrical specimens that can be considered as in 2D, flat specimens were considered to better analyse the 3D effect. Indeed, the spatial distributions of the measured variables with respect to the minimum width and the thickness was systematically studied.

2.3. Testing methods

2.3.1. Laboratory tensile tests

Tensile tests were carried out at the Centre for Material Sciences facilities using an electro-mechanic Instron machine (Instron 5982) with a load-cell of 250 N. An environmental chamber, Instron 3119-406 with temperature ranging from −100 to 350 °C, to run tests at low temperature, was installed. In order to follow the morphology evolution during the tests, the tests were instrumented with a Digital Image Correlation system (DIC). At low temperature, images were acquired through the furnace window.

Monotonic tensile tests were run up to failure under a crosshead speed of 250 μm/s at both low and room temperature (20 °C) and at a relative humidity of 50%. Both the load F and the displacement d versus time t were recorded during the tensile tests. The DIC system, composed of one Manta G-419B camera, 2048 × 2048 pixels, with Schneider Xenoplan 2.8/50 M30.5 lens, was synchronised with the data from the testing machine. The camera was placed perpendicularly to the specimen width focused on the gauge length. The image acquisition rate was equal to 120 fps. From these acquired images, the notch opening displacement NOD, the notch minimal width, and the notch root radii, were measured at the lateral surface, all along the loading.

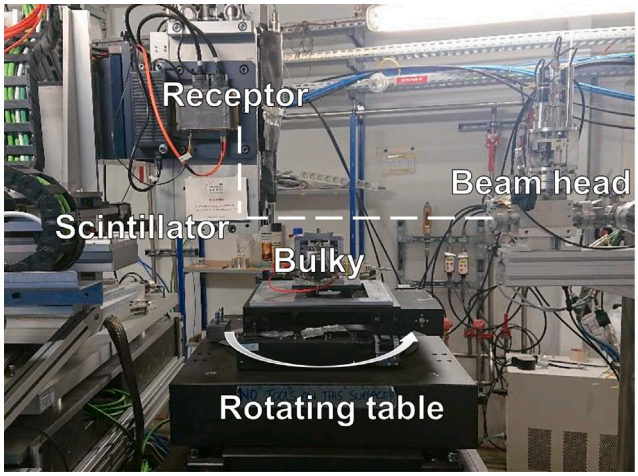

Fig. 3. Bulky rig at the PSICHE beamline of the SOLEIL synchrotron.

2.3.2. Tomographic in-situ tensile tests

Tomography by synchrotron radiation is an advanced imaging technique that leverages the high-intensity and highly collimated X-ray beams produced by synchrotron light sources. This method allows 3D imaging of the microstructure of a given material. The sample to be imaged is mounted on a rotating stage and then exposed to the X-ray beam. As the X-rays pass through the sample, they are absorbed and scattered to varying degrees, depending on the density and composition of the material. As the sample rotates, thousands of 2D radiographic images are captured at different angles using a detector positioned on the opposite side of the X-ray source. The 2D images are processed using computational algorithms to reconstruct a 3D virtual data set, *i.e.* 3D grey-level numerical objects. For a 16-bit volume, each voxel is characterised by a grey-level between 0 and 65 535, respectively black and white. Accordingly, an image is characterised by grey-level per voxel. Variations in grey-level are associated with the density crossed by the X-ray beam in the sample's microstructure.

In-situ tensile tests were carried out at PSICHE beamline of the SOLEIL synchrotron radiation facility using a pink beam — specific wavelength equal to 25 keV. Using a classical setup comprising a scintillator coupled to a x5 eye piece and a CMOS Hamamatsu camera, an effective voxel size of 1.3 μm for a field view 2 × 2 mm wide

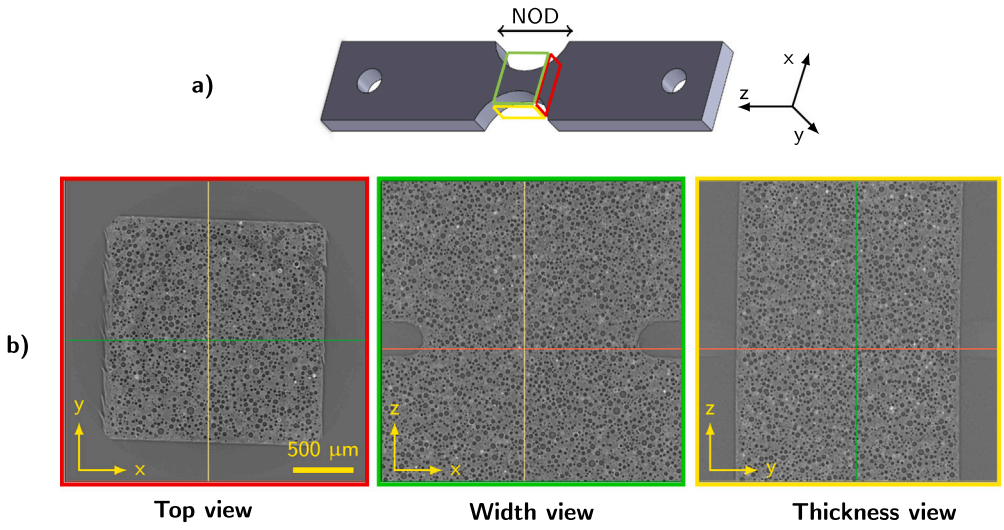

Fig. 4. Description of a tomographic data set for a GSPP sample: (a) volume in the central part of a N_4 specimen; (b) virtual cuts for top view (in red — xy plane), width view (in green — xz plane) and thickness view (in yellow — yz plane). (For interpretation of the references to colour in this figure legend, the reader is referred to the web version of this article.)

by 2 mm in height was obtained (Fig. 3). In-line phase contrast and Paganin filtering of the radiographs [23] were used to enhance image contrast by placing the camera 65 mm downstream from the sample. Tomographic reconstruction was carried out using PyHST software and further processed [24].

The testing machine Bulky [25] – rig primarily used for X-ray tomography under continuous loading – was used. The mechanical design was made to test specimens up to 5 kN (for high-yield strength steels or titanium alloys) and with a mechanical stroke of 15 mm (for ductile metals and polymers). The high-torque stepper motor moves the crosshead with an adjustable speed ranging from 50 nm/s to 0.5 mm/s. A wide range of different assemblies can be installed to adapt the machine to different configurations [26]. The Bulky rig was fixed to the pivoting platform (rotating table), see [26] for more details. In addition to pivoting, the platform is equipped with a height corrector which allows the platform to be moved vertically in order to keep the notch at a constant position, in spite of its displacement due to the local deformation.

In-situ stepwise tensile tests were carried out up to failure using two crosshead speeds: 1 µm/s for loading, but changed to 0.05 µm/s during the tomography acquisitions. Indeed, a lower crosshead speed, rather than a holding time, allows a better acquisition while avoiding the viscoelastic effects. Height correction was used to keep the notched region within the field of view. For tomography acquisitions, the platform was set to rotate continuously while tomography data sets were acquired in 6 s. Each tomogram is composed of a thousand radiographs equally distributed over a half-turn (only one half of the detector height was used to speed up the data collection). An *in-house* Python script, running in a beamline control terminal, automatically executed the progress of a mechanical test, coordinating all motor movements, acquiring the relevant signals, managing the tomography acquisitions and stopping when the specimen breaks [26]. The data acquisition strategy was user-controlled, this allowed direct control of the tomography frequency. As a matter of fact, the tests using the Bulky stress rig correspond to low-speed tests, therefore no significant temperature rise is expected [27].

2.3.3. Tomographic data sets

Fig. 4a illustrates a tomographic data set located at the notched zone of a N_4 specimen of GSPP. The volume of interest is characterised by the transparent box. Three planes of various colours (red, green and yellow) are indicated in Fig. 4b, so as to symbolise the virtual cuts that will be exploited in the following. The tomographic views being at the same scale in all figures, for the sake of clarity, the scale bar is shown at once in one image for each figure.

Actually, reconstructed data sets were cylindrical with both diameter and height of 2 mm. Voids are reasonably well-defined in dark grey whereas PP bulk appears in grey. Indeed, in the unloaded condition, the voids correspond to the empty space inside the microspheres whereas, during loading, they can also correspond to the cavities within the PP matrix or the HGM-PP matrix debonding. In addition, white features are associated with the phase contrast of the HGM-bulk interface, *i.e.* the white halos can be seen as the thickness of the glass microspheres. Qualitative analysis of dimension, morphology and spatial distribution of voids, both cavities within the bulk and debonding, are then allowed.

The tomographic volumes were studied using Fiji [28] and Avizo software [29]. Thickness-direction and loading-direction sweeps were made on each tomographic volume of interest. The threshold levels were adjusted by hand to improve the visualisation. In order to handle easily the tomographic volumes, Python scripts were developed to cut-out sub-volumes of interest from the raw data.

3. Results and discussion

In this section, *in situ* tensile tests are exploited. Analysis of the tomographic data set allows gathering both the width and thickness evolution in the minimum cross section, and the notch opening displacement (nod) during the tests. However, the nod of the N_4 specimen was not accessible as the notch borders were situated outside the tomographic field of view. Therefore, in the following, the nod of N_4 specimens was replaced by that of preliminary tensile tests at the laboratory facilities.

For each *in situ* test, the tomographic data sets will refer to the load *vs.* nod, to situate the load level of the specimen. In order to retrieve the trend of the microstructure evolution, only a few number of tomographic volumes was studied. Nevertheless, the points of interest in the load *vs.* nod, *i.e.* the load corresponding to the deviation from the linearity, the maximum load and the load at failure, were taken into account. A qualitative study of the microstructure evolution in the net cross section during deformation is then proposed. Thanks to *in situ* 3D imaging, the data sets combine the spatial distribution of the observed pattern and its evolution, in real time, with respect to the applied displacement.

In the following, the figures are based first on the load F, normalised by the maximum load F_{max}, plotted with respect to the

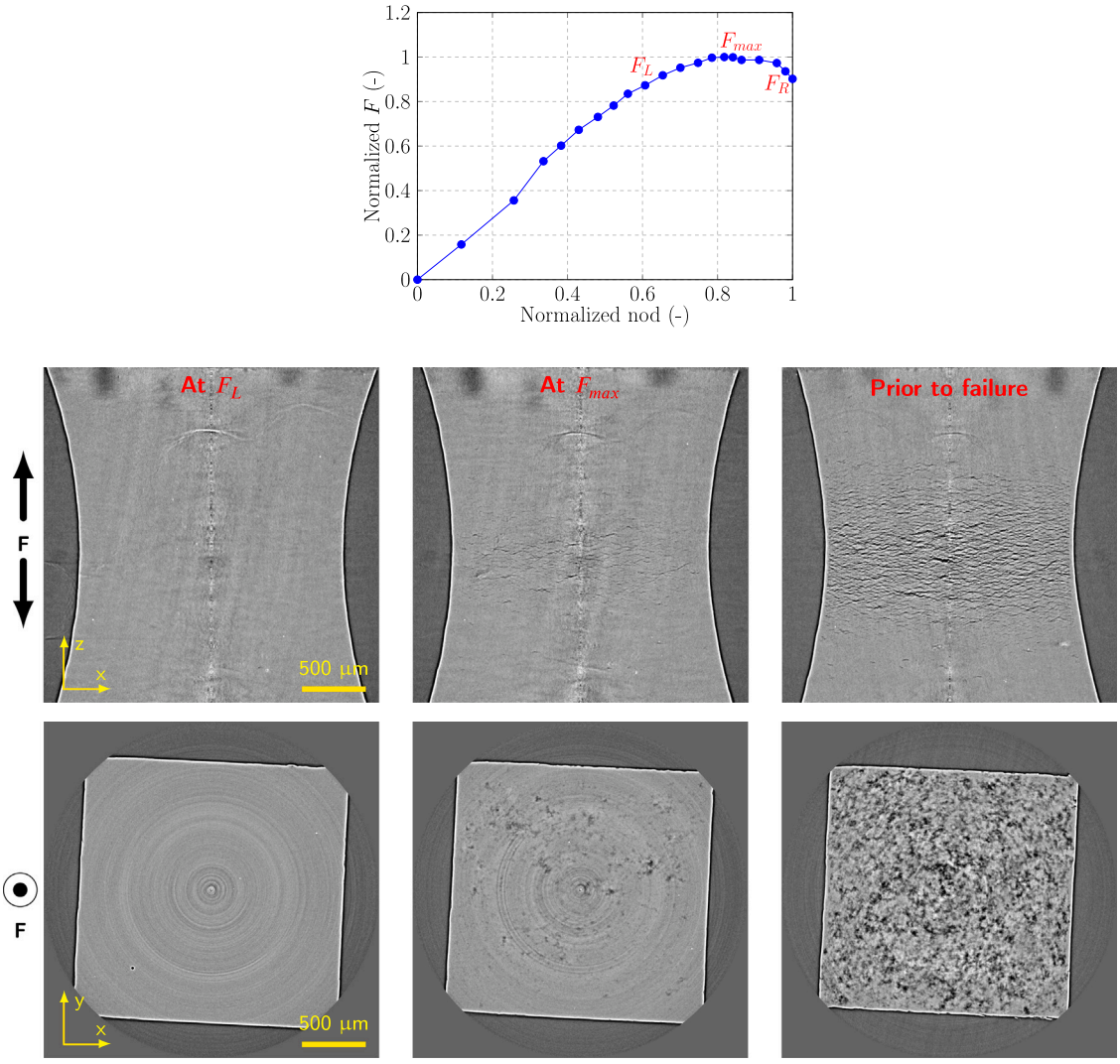

Fig. 5. Mechanisms of craze appearance and growth during *in situ* test on PP N_4 specimen.

normalised nod, by the nod at failure. The limit load F_L was identified as the point where the deviation from the linearity was estimated to appear and F_R is indicated as the load at failure. Then, the views corresponding to the points of interest in the load *vs.* nod curve are displayed so as to analyse the change in the microstructure.

Due to confidentiality restrictions, the parameters of normalisation such as the maximum load and the notch opening displacement at failure are not given here. However, each point of interest can be easily identified on each load *vs.* nod curve.

3.1. Neat PolyPropylene

The observation of the tomographic volumes, in the semi-crystalline polymers like PP, allowed the analysis of the deformation and cavitation mechanisms leading to the appearance of crazes in the plane orthogonal to the loading direction [30]. As these crazes are zones of lower matrix density, they appear darker in the tomographic volumes. Generally, they are located at mid-thickness [22,31–33].

For semi-crystalline polymers such as PP, reducing the notch root radius results in an increase in stiffness, and therefore the maximum load [22,34,35]. This also leads to changes in the shape of the force, the notch opening displacement, the width reduction as well as the thickness reduction according to the applied displacement. The main observable change in the bulk concerns the location of the maximum void volume fraction: at mid-thickness and mid-width in the N_4 like specimens, whereas, at mid-thickness and close to the notch root for the $N_{0.15}$ like specimens [30]. Therefore, this location depends on the triaxiality ratio induced by the notch root radius [32,36,37].

3.1.1. N_4 specimen

In Fig. 5 the normalised load *vs.* nod curve of N_4 specimen shows the position of the limit load F_L, the maximum load F_{max} and the load at failure F_R. A load softening stage is noticed after F_{max} and a sudden drop of the load is observed just after F_R. The tomographic views at these three points of interest follow the plot. The width views, corresponding to the mid-thickness plane, are plotted before the top views.

The tomographic volumes were studied using Avizo software [29]. The side of each view corresponds to 2048 pixels, *i.e.* 2662 µm. In all the prescribed views, the surface border could be easily identified thanks to the contrast between the material and the free space. Some circular artifacts (ring artifacts), associated with the acquisition technique, are visible especially in the top views. The effect of these artifacts is negligible on a qualitative study. Furthermore, no significant effects have been reported in quantitative studies [38,39]. Recall that dark grey pixels correspond to less dense matter.

At F_L, similar to initial – non deformed – slices (not presented here), only artifacts could be seen as dark pixels. However, this apparent

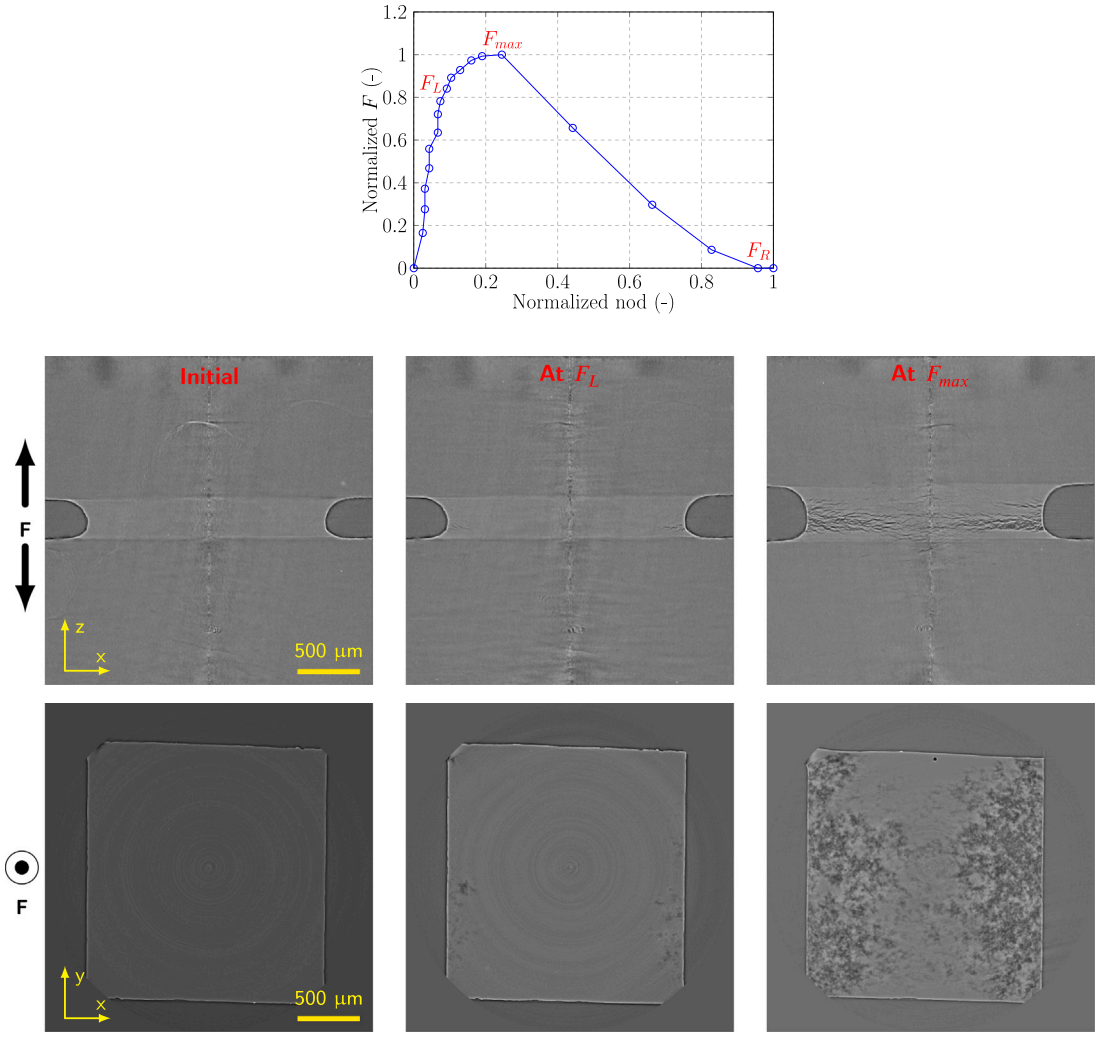

Fig. 6. Mechanisms of craze appearance and growth during *in situ* test on PP $N_{0.15}$ specimen.

absence of voided patterns could be related to the acquisition resolution (equal to 1.3 µm). Eventually, using a higher resolution, *e.g.* magnified synchrotron radiation holotomography [40], void features could be identified.

At F_{max}, in the middle column of tomographic views, some thin dark horizontal stripes, concentrated at mid-height, *i.e.* in the minimum notch section, appeared in the width view. In the corresponding top view, cut at the net section, these stripes are projected as black dots concentrated in the specimen core. These dark features are identified here as crazes, *i.e.* an ensemble of voids and fibrils of matter with penny shape perpendicular to the loading direction. No craze was visible near the notch surfaces and crazes with higher height seemed to be located at mid-width near the minimum notch section. In the right column, labelled as "Prior to Failure" corresponding to F_R, both width and top views showed more numerous crazes. When comparing the state of the microstructure with that at F_{max}, it could be observed that "new" crazes appeared and those which were already apparent at mid-height in the minimum notch section at F_{max} increased in height and diameter. The load softening, from F_{max} to F_R is likely to be related to the multiplication of crazes. Furthermore, the radial coalescence of these crazes was supposed to provoke the rapid failure of the specimen, leading to the sudden drop of the load. Note that the failure is due to a rapid crack growth from the centre to the lateral surface.

3.1.2. $N_{0.15}$ *specimen*

In Fig. 6 the tomographic volumes of $N_{0.15}$ during deformation are shown. The load *vs.* nod curve differs from that of N_4 in the final failure part. Indeed, here there was no load softening after F_{max} but the load drop-down is gradual. The stiffness seemed also to be higher for $N_{0.15}$.

The view at initial state (left column) allowed the artifacts to be identified. No other dark features were observed.

At the limit load F_L, see middle column in Fig. 6, sparse crazes appeared, identifiable as thin dark stripes, near the notch surface. The crazes are not situated at mid-height, but at the minimal cross section as the notch is not completely symmetric. Indeed, the bigger crazes seems to be situated at the root of the notch surface. No crazes were observed at the core of the specimen notch section. From the top view, it can be inferred that the crazes are concentrated at mid-thickness. Moreover, it seems that the size of crazes is higher at mid-thickness than at the borders. No crazes were observed near the border corresponding to the width surface. The gradual appearance of these crazes probably induces the non linearity in the load *vs.* nod curve, until reaching F_{max}.

At F_{max} (right column), just before the load drops down, the width view illustrates the multiplication and growth of crazes. Other crazes appeared around the pre-existing ones at F_L, at the notch roots. Moreover, these pre-existing crazes grew from the notch root towards the specimen core. The concentration of the crazes near the notch root was verified in the top view. The maximum concentration seeming to be located at mid-thickness.

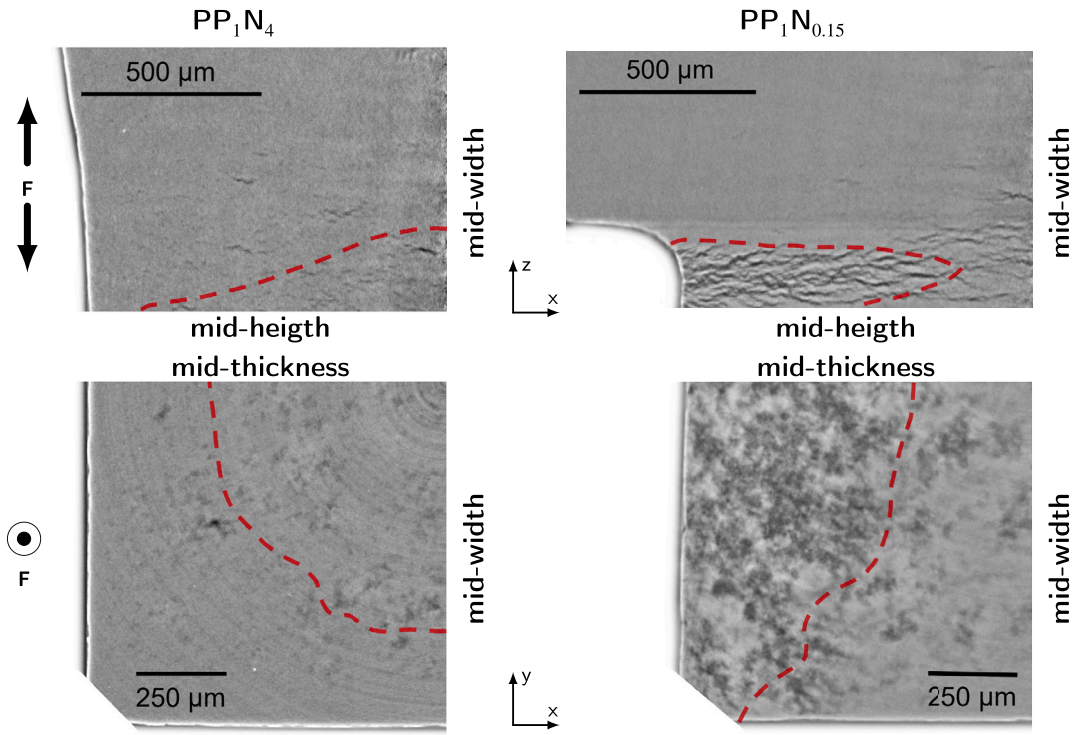

Fig. 7. Localisation of maximum crazes at the maximum load F_{max} for N_4 and $N_{0.15}$ specimens. Width and top views were displayed respectively at the top and bottom of the figure.

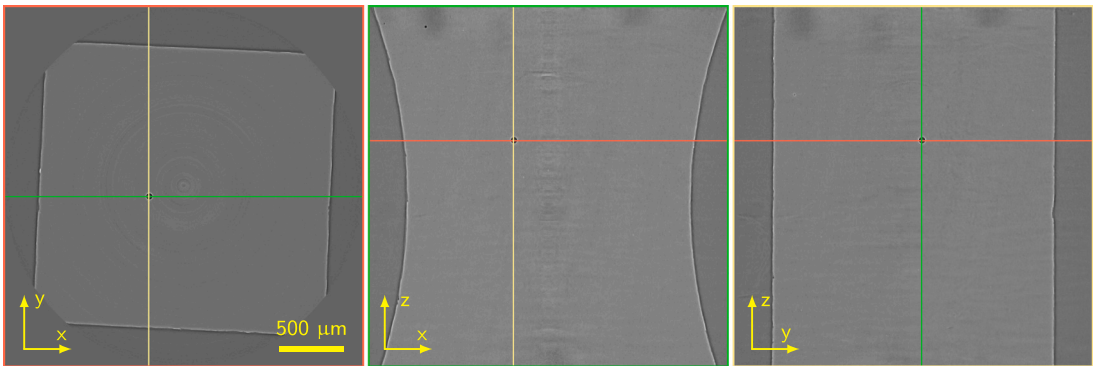

Fig. 8. Embedded single hollow glass microsphere (SHGM) in the central part of N_4 specimen: Top, width, and thickness views (from left to right).

Beyond F_{max}, the tomographic volumes showed a principal crack which propagated until the load reached zero value. It can be concluded that $N_{0.15}$specimen mimicked fracture mechanics specimen with pre-crack. This topic is out of the scope of the present work.

3.1.3. Summary for neat PP matrix

The distribution of the crazes on N_4 and $N_{0.15}$ specimens at the maximum load is highlighted in Fig. 7. Width and top views are respectively shown at the top and at the bottom of the figure. The slices correspond to the views at mid-thickness (width views) and at the minimum cross section (top views). Red-dashed lines were used to identify the localisation of the crazes in the net section. The crazes were concentrated at the notched volume, at mid-height, in both geometries. However, the crazes were located in a different position along the width. Indeed, crazes were located at the specimen core in N_4 specimen, whereas, in $N_{0.15}$ specimen, they were located at the notch root. From the top view, a concentric distribution of the crazes was noticed in the N_4 specimen. Indeed, more and bigger crazes were observed at the core centre. Besides, concentration of the crazes on the notch roots was observed in $N_{0.15}$. More and bigger crazes seemed to be located at mid-thickness. The observations at the maximum load were completely in line with previous observations on polyamides [22,30,32] and, even, on an epoxy resin thermoset [33].

3.2. PP-embedded single hollow glass microsphere

During the image analysis of the tomographic volumes of PP some isolated Hollow Glass Microspheres (HGM), embedded in the matrix, were noticed. We took advantage of them so as to follow the same planes containing a single HGM (SHGM) during the whole loading. Furthermore, attempts were made to study the interaction between the crazes in the matrix, as described above, and the mechanisms of decohesion of the SHGM and the PP matrix in the notched region submitted to triaxial stress state. In other words, the aim consisted of studying experimentally the local kinematics of an isolated SHGM within a "infinite" matrix. Therefore, some well positioned SHGMs

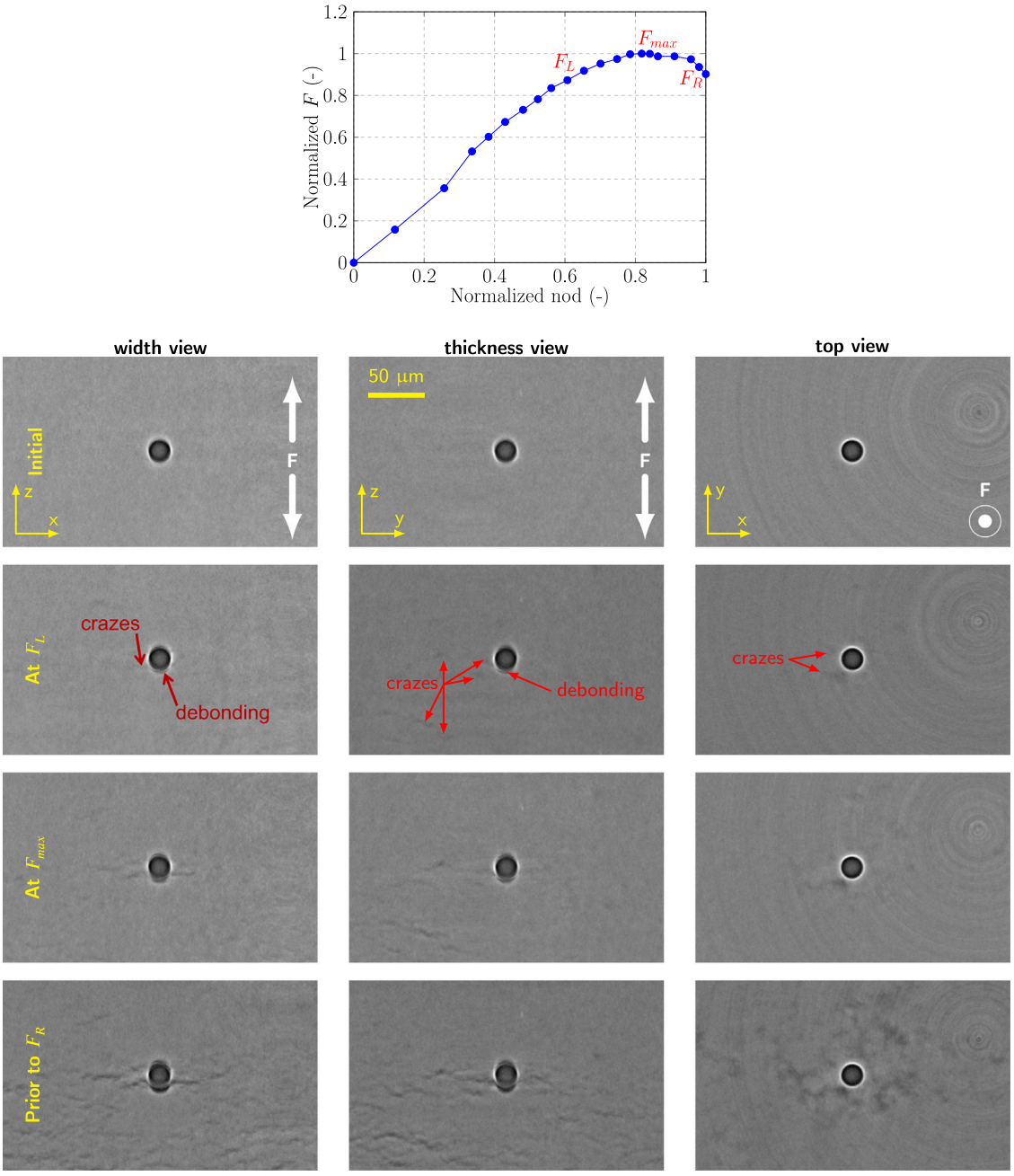

Fig. 9. Chronology of crazing and SHGM decohesion mechanisms inside the N_4 specimen. *SHGM diameter* = 22 µm.

were selected inside each of the two geometries. It should be noted that the same load *vs.* nod curves were involved because the following data sets analyses were carried out from the same *in situ* tests. Additionally, as these spheres were sufficiently distant from each other, no interaction between them could reasonably be expected.

3.2.1. N_4 *specimen*

Position of the microsphere for N_4

The position of the SHGM in the N_4 specimen is shown in Fig. 8. It was located at the mid-thickness and approximately at mid-width where the maximum concentration of crazes occurred (see Fig. 5). A small gap equal to 400 µm, between the minimum cross section and the horizontal plane of the SHGM, was noticed. As no additional spheres have been observed after sweeping in the thickness and the width directions, no interaction between micro-spheres could be expected. This specific SHGM has a diameter of 22 µm. The change of the microstructure surrounding it will be studied in the following.

Evolution of the microstructure around the SHGM for N_4 *specimen*

In Fig. 9 the crazes, in the PP matrix, and the SHGM decohesion mechanisms during the N_4 *in situ* tensile test are shown. As mentioned before, the same load *vs.* nod curve as in Fig. 5 was reproduced here to easily correlate the three main views (width, thickness and top), with the progress of the loading in the test. The thickness view was added to the width and top views at each corresponding increment of loading, so as to give more details around the SHGM.

The initial state showed once again the ring artifacts on the top view. In addition, at the present resolution of 1.3 µm, the three views

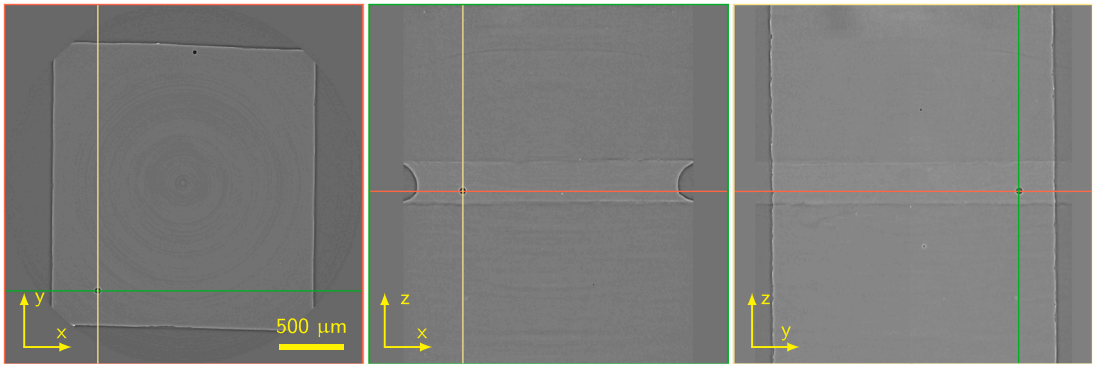

Fig. 10. Embedded single hollow glass microsphere (SHGM) inside the notched region for the $N_{0.15}$ specimen: Top, width, and thickness views (from left to right).

were magnified so as to better study the grey levels changes around the SHGM within the PP matrix.

At F_L, crazes could be identified as lightly darkened grey levels in the matrix whereas the SHGM-matrix decohesion could be detected as a loss of contrast on the perimeter of the sphere, together with a darkening of the poles of the sphere. A formation of a sickle-shaped cap was observed, to be linked to voiding due to matrix-sphere decohesion. The views were annotated to better understand the slight changes in grey level. Red arrows indicate the patterns identified as decohesion and crazes (or single void). Therefore, in the width view, debonding and craze were identified together as indicated by the red arrows. At these resolution and magnification, the decohesion and the craze formation seemed to appear at the same time. Indeed, by opposition to Fig. 5 at F_L, crazes are more visible here. In the thickness view, more crazes were distinguished and the debonding at the "south" pole is still visible, confirming the cap shaped void due to the debonding. In the top view, no debonding was visible at the equatorial region of the SHGM. Crazes were also identified as darkened zones which had more surface than the stripes in the width and thickness views.

At F_{max}, it was observed an appearance of new crazes and darkening and propagation of pre-existing crazes, especially in the thickness view. The pre-existing crazes were indicated by the red arrows in the previous views at F_L. SHGM-matrix decohesion was observed in both poles. They seem to stop at a given angle (tropic above/under equator) forming spherical caps at the two poles of the SHGM. Coalescence of craze and decohesion void was observed at the circular end of the cap in the width view. The SHGM at the equator level is still in contact with the polymer matrix. The adhesion could be verified in the top view, where the crazes are surrounding the sphere but without *touching* the surface. In addition, in the top view, the crazes as darkened patches were more discernible in comparison with those seen at F_L. Note also that in Fig. 5 at F_{max} the crazes were mentioned to be visible at less magnification.

Prior to failure, propagation of both crazes already coalesced with the decohesion, and considered as "independent" (formed in the bulk of the matrix), was observed. The maximum crazes were located perpendicularly to the loading axis and in the notch plane, especially in the matrix under the SHGM. Moreover, in the top view, these crazes were visible around the entire circumference of the sphere. As this view corresponds to the plane of the equator, the places where the crazes meet form a darker halo around the bright circle around the SHGM. These results are in accordance with previous comments about the crazes distribution in Fig. 5 on PP N_4. The radial coalescence of crazes in the notch plane formed a crack which quickly propagated from the centre to the notch root at the surface, causing the rapid failure of the whole specimen.

3.2.2. $N_{0.15}$ *specimen*

Position of the microsphere for $N_{0.15}$

The position of the SHGM in the $N_{0.15}$ specimen is identified in Fig. 10, at the intersection of the two perpendicular lines for each view. Top, width, and thickness views of the $N_{0.15}$ notch are illustrated from the left to the right. The SHGM was located at the notch-root plane, *i.e.* the minimum cross-section. The distance between the left notch root and the SHGM was about 250 µm. The diameter is approximately the same as the one of Fig. 8. Additionally, this SHGM was not positioned near the mid-thickness plane but at 320 µm from the width surface. It is then well placed inside the crazed-zone highlighted in Fig. 6 corresponding to PP $N_{0.15}$ specimen. An additional but smaller SHGM could be noticed at mid-plane, top view. It was located far away from the aforementioned one. No interaction between the two spheres was expected to occur.

Evolution of the microstructure around the SHGM for $N_{0.15}$ *specimen*

In Fig. 11 the crazes, in the PP matrix, and the SHGM decohesion mechanisms during the $N_{0.15}$ *in situ* tensile test are shown. The load *vs.* nod curve was included so as to easily synchronise the views with respect to the loading increment. It should be recalled that the same load *vs.* nod curve was plotted in Fig. 6. Namely, the specific shape of the curve showed a progressive decrease in force after F_{max}, down to F_R. Some intermediate views were included so as to better analyse the major changes in the microstructure. Per line, the width, thickness and top views were displayed from the left to the right, *i.e.* column 1 to 3.

In the initial width and thickness views, only the marks of the notch shoulder are visible as dark stripes above and beneath the SHGM. For the top view (right), this is represented by the oriented line in bottom left. The SHGM is clearly visible, especially the bright halo of the glass hollow sphere. For the thickness view, the proximity of the SHGM to the free surface makes that this width surface plane is visible as a vertical line in the right side of the view. The plane at mid-thickness being then situated far away but on the left side of the view. For the top view, the edge of the cylindrical tomographic volume makes appear the oriented line at bottom left of the view. The plane at mid-thickness is located beyond the left side of the top view. These indications would help to better understand the mechanisms of crazing and debonding described in the following.

The next line of views corresponds to the state of the microstructure just prior to F_L, *i.e.* at $0.7F_{max}$. Whereas no contrast could be discerned above and below the SHGM, some crazes emanating from the notch were observed as slight dark stripes, beneath the word "crazes" in the width view. The tip of the longest craze in this cutting plane was indicated by the red arrow. It did not reach the SHGM. It can be deduced that the range of the stress singularity induced by the notch root was less than the distance to the SHGM. At the same time, the free surface on the right side in the thickness view remained straight. For the top view, crazes were visible on the top left area, in the region indicated by the word "crazes".

At F_L, a new craze – labelled "craze from debonding" – appeared at the left notch, seeming then to propagate towards the notch root. By contrast to the situation for N_4(Fig. 9 at F_L), it was not possible to confirm whether the decohesion was first than the craze propagation, or there was some simultaneous crazing/decohesion coalescence. Indeed,

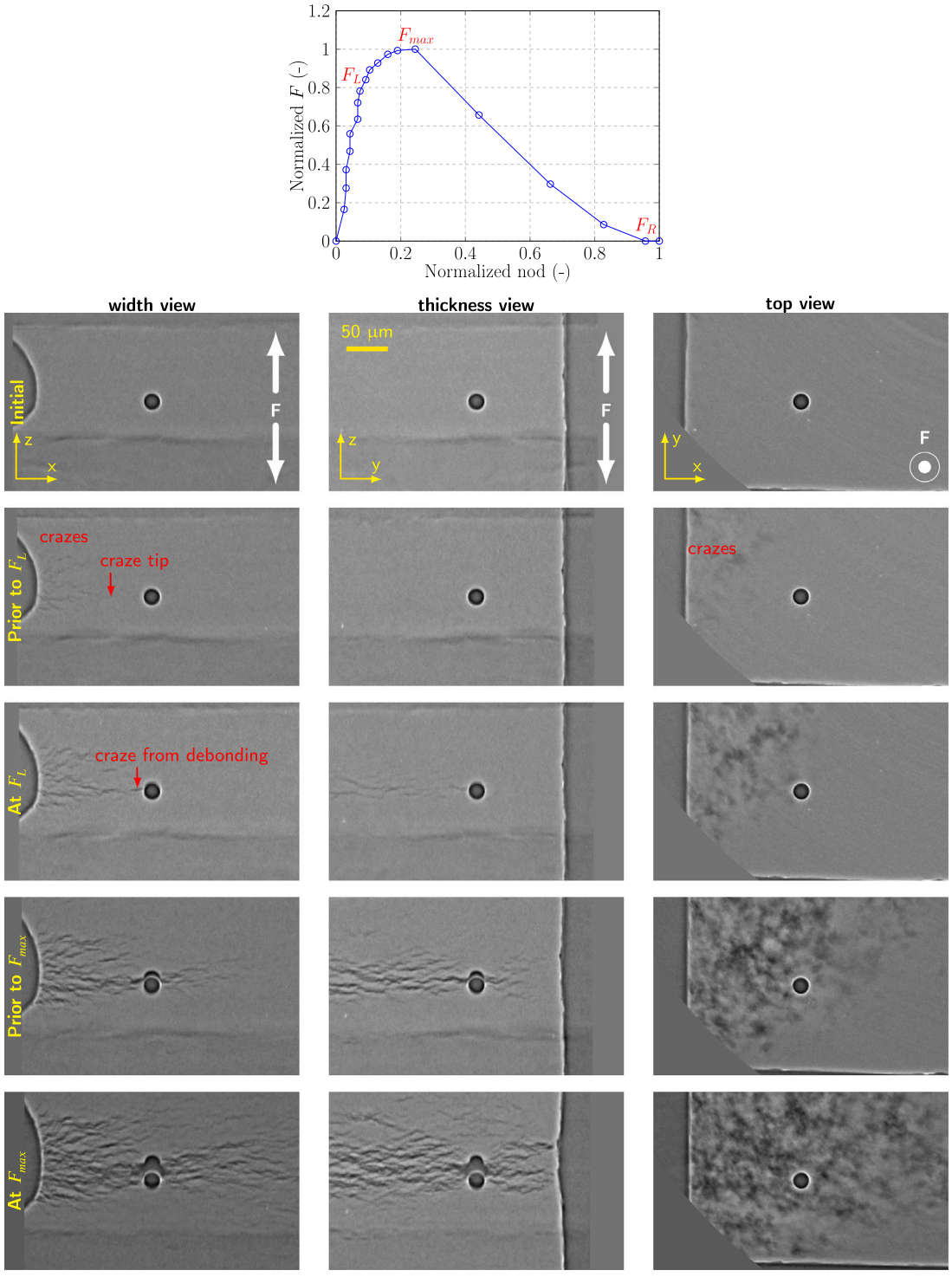

Fig. 11. Craze-SHGM decohesion mechanisms in the $N_{0.15}$ specimen.

the debonding could not be clearly observed, through this cut, although, a slight "perturbation" of the bright halo could be distinguished at the north pole of the SHGM. The previous longest craze "darkened" (due to void growth) and increased in length. Its tip moved towards the SHGM and was situated beneath the new craze from debonding. It seems then that due to the limited stress range, the stress level around the SHGM was not enough to trigger the debonding. In the thickness view a part of the craze from debonding is also visible. The cluster of crazes could be observed on the left side of the SHGM, confirming again that the maximum of crazes is situated close to the mid-thickness plane. So is the situation for the top view. But the crazes are subjected to darkening and multiplication.

The next three views labelled as "Prior to F_{max}" clearly showed the craze from decohesion crossing the SHGM by the north-pole. Indeed, the craze from debonding was visible all around the north pole of the SGHM as illustrated by: (i) the width view, since part of the craze

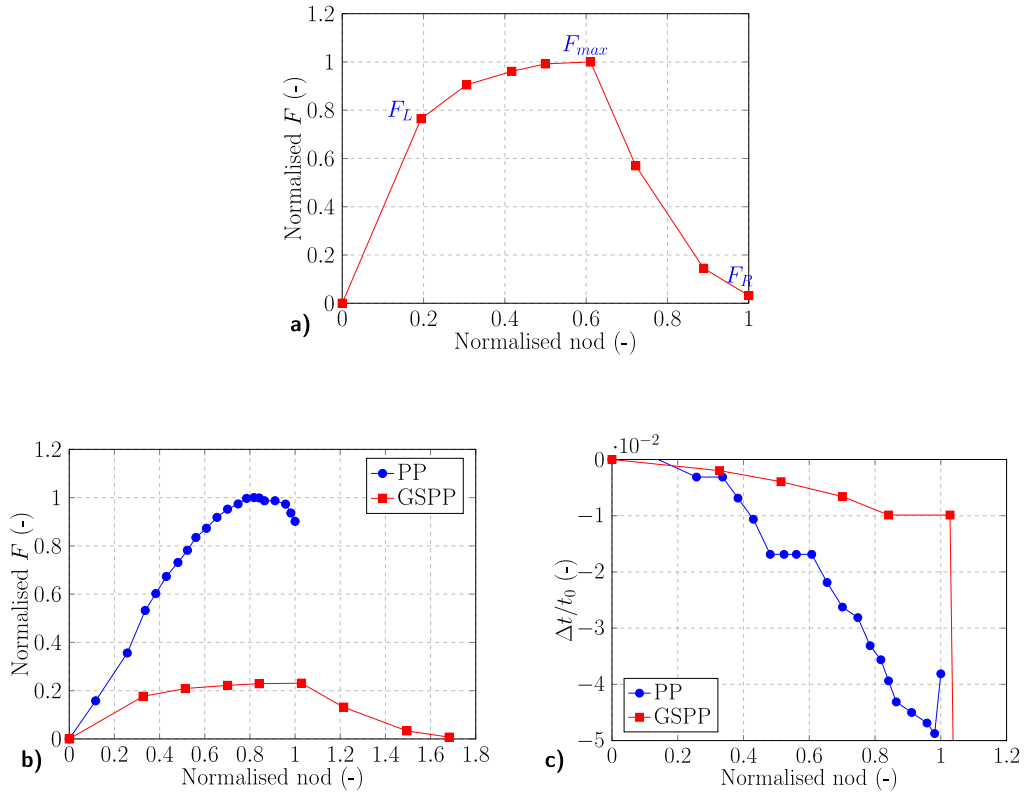

Fig. 12. Specific curves for N_4 specimens: (a) F-nod curve for GSPP; (b) Comparison between F-nod curves for PP and GSPP; (c) Comparison between the thickness reductions ($\Delta t/t_0$) for PP and GSPP.

appeared on the right side of the SHGM; (ii) the thickness view, where the cap is surrounded by crazes. Coalescence between the crazes and the decohesion is then clearly highlighted. Furthermore, the thickness view showed that some crazes appeared on the right side of the SHGM without reaching the free surface. The crazed zone entered the plane stress region at this stage. The vertical line corresponding to the free surface becomes curved around the horizontal plane where the crazes are situated. The top view shows again that the darkened patches cross the SHGM, for which no debonding appeared at the equatorial region (intact bright halo).

At F_{max} the debonding cap has become a great void inside a very crazed zone. Indeed, from width and thickness views, the SHGM is completely debonded at the north pole but partly debonded at the south pole. However, it seems that it is still in contact with the polymer matrix at the equator level. From top view, this assumption could be checked since a significant contrast between both the polymer matrix and the SHGM surface was observed. The SHGM is completely surrounded by the crazes; however, no effect on the sphere was noticed, *i.e.* no failure of the SHGM was inferred. In the thickness view, the crazes' tips reached the free surface, causing a thickness necking. Darkening, multiplication and propagation of all crazes were enhanced. A main penny shaped crack is likely to appear at the plane at mid-thickness [32]. This crack should propagate towards three directions: through the width and the two lateral directions. The gradual decrease in the load after F_{max} is attributed to this crack growth.

3.2.3. Summary for PP-embedded single hollow glass microsphere

- Mechanisms of crazing in the PP matrix and debonding at the poles of SHGM were highlighted;
- The appearance of the debonding depends on the stress level around the SHGM when embedded inside a matrix subjected to stress triaxiality and gradient;
- Depending on the notch root radius the location of both phenomena differed:
  - At mid-thickness and mid-width for N_4;
  - At mid-thickness and at a small distance ahead of the notch root for $N_{0.15}$;

3.3. Results on Glass Syntactic PolyPropylene (GSPP)

This section deals with the Glass Syntactic PolyPropylene (GSPP) investigation on the two specific specimens, respectively $N_4$and $N_{0.15}$. After having studied the decohesion and crazing mechanisms in isolated spheres, focus is put on the mechanisms in the GSPP specimens, where the interaction between spheres must be accounted for. The objective is then to highlight the main effects of the addition of 30% volume fraction of HGMs' into the matrix.

3.3.1. N_4 specimen

For tomographic *in situ* test on GSPP N_4 specimen, the load and displacements measured during the loading were first analysed. Then, the mechanisms of crazing-decohesion were studied thanks to the examinations of the tomographic data sets, as already be done for the PP with SHGM.

Comparison between specific curves for PP and GSPP for N_4 *specimen*

Fig. 12 displays the specific curves of GSPP N_4. First, Fig. 12(a) shows, as previously used for PP, the load *vs.* nod normalised respectively by its own maximum load and nod at failure. This curve shows three specific events labelled F_L, F_{max} and F_R. This latter corresponds to the point of last data set recorded, where the load was near zero.

In Fig. 12b, a comparison between the F-nod curves of PP and GSPP was attempted. To allow this comparison, the loads and nods' were respectively normalised by the maximum load and nod at failure of PP. It can be highlighted that F_{max} and the nod at failure of the

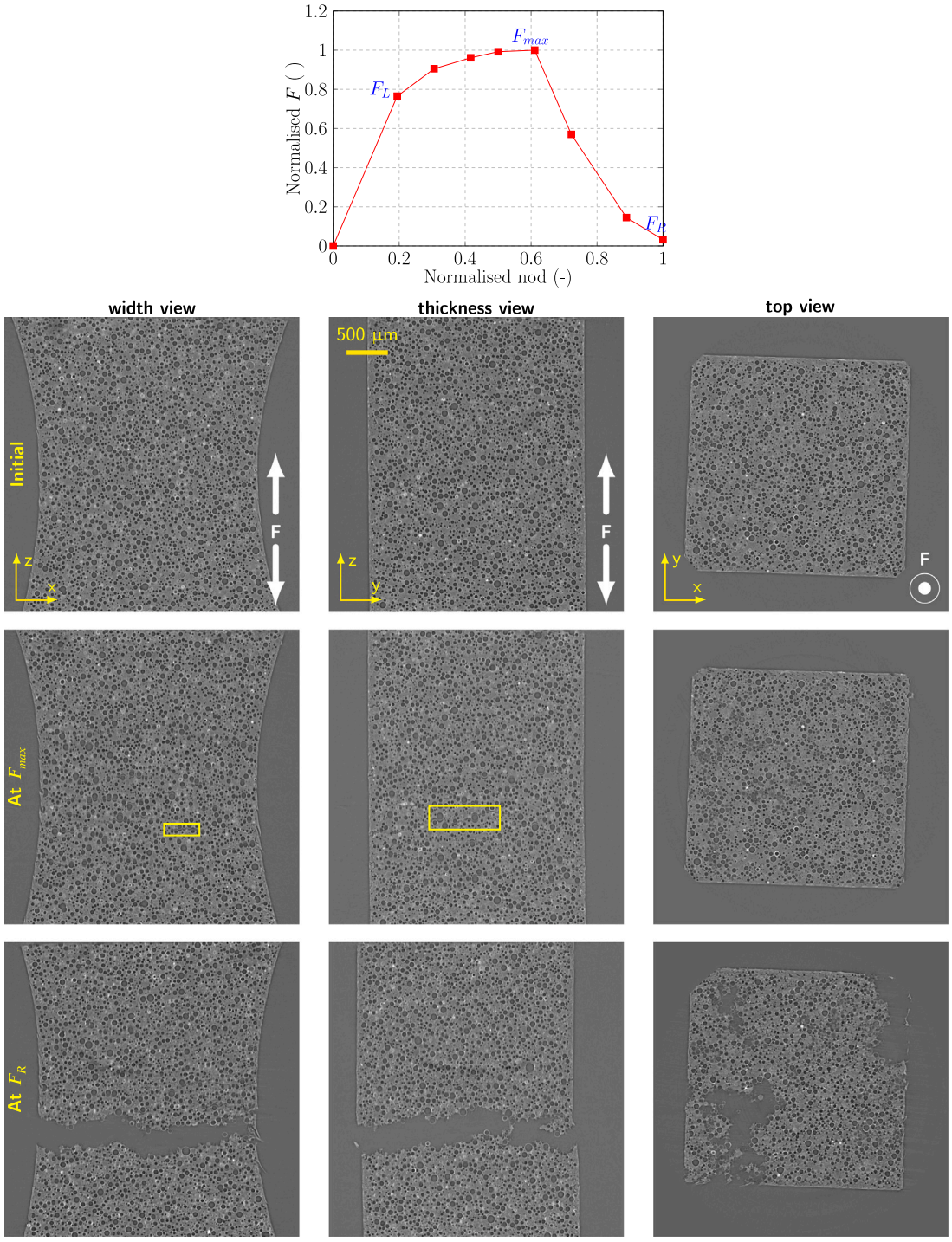

Fig. 13. Mechanisms of decohesion in the GSPP N_4 specimen.

GSPP were, respectively, 5 times lower and 1.7 times higher, than that of PP. Furthermore, GSPP exhibited a gradual decrease in the load during the failure stage (after F_{max}).

3D-imaging allowed the measurement of the thickness reduction ($\Delta t/t_0$) in both materials PP and GSPP. The same normalised nod, as in Fig. 12b, was used in the abscissa axis, but the range was reduced to 1.2 (approximately the nod at failure of PP). A noticeable difference in $\Delta t/t_0$ magnitudes was observed (Fig. 12c). Namely, at failure of the PP the nod was 5 times higher in absolute value than that of GSPP. This can be related to a higher volume increase in the GSPP in comparison with that of PP.

Evolution of the microstructure for GSPP N_4 specimen

The first line of Fig. 13 reproduces the same load *vs.* nod curve in Fig. 12a. The limit load F_L, the maximum load F_{max} and the load at failure F_R are characterised in this curve. Like in PP results, the three views (width, thickness and top) are displayed, for GSPP at the three selected events in the prescribed load *vs.* nod curve.

The initial microstructure shows the distribution of the 30% volume fraction of microspheres. In the three views the surface border is easily identifiable thanks to the contrast between the material and the free space. As a matter of fact, both the width and thickness reduction could be measured “by hand”, using image treatment techniques, from these

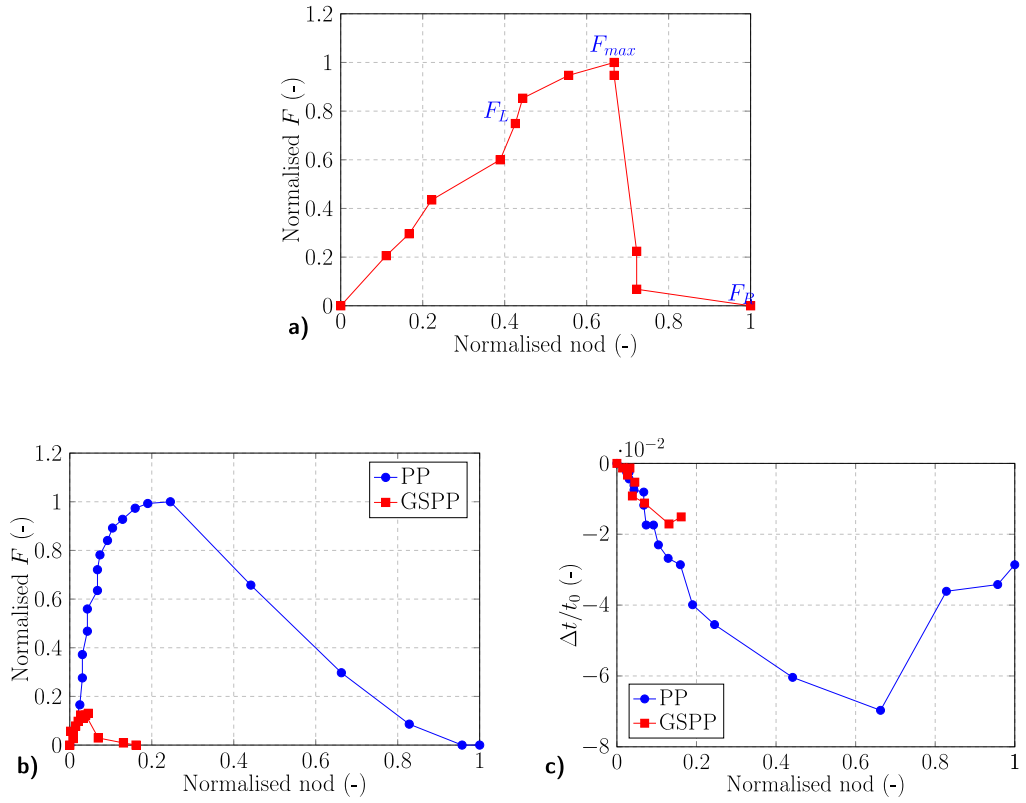

Fig. 14. Specific curves for $N_{0.15}$ specimens: (a) F-nod curve for GSPP; (b) Comparison between F-nod curves for PP and GSPP; (c) Comparison between the thickness reductions ($\Delta t/t_0$) for PP and GSPP.

data sets. No ring artifacts, associated with the acquisition technique, were visible. The microstructure shows a random distribution of Hollow Glass Microspheres (HGM) of various sizes but overall homogeneous in the distribution. These spheres appear as white halos surrounding dark discs. The polymer matrix is visible in light grey.

Crushed microspheres, linked with the extrusion process, could be assumed by the presence of debris in the matrix. However, their existence seem to have no impact on the initiation and crack propagation during the tensile test.

At F_L there is not so much change in the microstructure, at this magnification. Accordingly, the corresponding views were skipped.

At F_{max}, several decohesion caps are visible in the width and thickness views. In the width view, a series of seven coalesced caps was surrounded by the yellow rectangle. The same patterns could be observed in the thickness view, inside the yellow rectangle. A magnified view of these coalescence of caps will be proposed later. Otherwise, using a higher resolution, *e.g.* magnified synchrotron radiation holotomography [40], would help to make the decohesions clearer. These coalescences of decohesion caps appeared in the central region of the notched volume. From the top view, these decohesion caps could not be clearly identified. One can just distinguish some darkened areas which can be attributed to these coalescences. These latter could be attributed to grey halos surrounding HGMs.

At F_R, the crack is clearly identified in the net section through the three views. As discussed before, the crack probably initiated in the central region of the notch and propagated to the free surfaces. Additionally, no microsphere break was noticed in the whole data sets.

3.3.2. $N_{0.15}$ *specimen*

Comparison between specific curves for PP and GSPP for $N_{0.15}$ *specimen*

Following the same approach as for N_4 , Fig. 14a displays the normalised load *vs.* nod of GSPP $N_{0.15}$. Recall that for this curve the normalisation was operated by using the own maximum load and nod at failure of the test. Once again, three specific events were highlighted in this curve: F_L, F_{max} and F_R.

In Fig. 14b, the load and nod were normalised with respect to F_{max} and the nod at failure of the PP to allow the comparison. Whilst the shape of the curves was similar, a drastic decrease in F_{max} and the node at failure was observed when comparing the PP with the GSPP materials. In both variables, a factor 5 of decrease was observed. This was in contrast with N_4 specimen (Fig. 12b) where the nod at failure for GSPP increased with a factor 1.7 compared with that of PP.

The comparison of the thickness reduction ($\Delta t/t_0$) in both materials PP and GSPP is illustrated in Fig. 14c. The same but inverted trend could be noticed between Figs. 14b and c. As a matter of fact, the initial (up to −2%) slope was similar, until the early failure of the GSPP.

From Fig. 14, a significant embrittlement of GSPP was evidenced due to the addition of HGM in the matrix.

Evolution of the microstructure for GSPP $N_{0.15}$ *specimen*

Fig. 15 reproduces, on the top, the same load *vs.* nod curve in Fig. 14a, where the limit load F_L, the maximum load F_{max} and the load at failure F_R were indicated. The width, thickness and top views were displayed, for GSPP at the three selected events in the prescribed load *vs.* nod curve.

The initial microstructure is similar to that of the N_4 specimen (Fig. 13) apart from the shoulders of the notches, as they were clearly visible here. There is no ring artifacts due to the acquisition technique. The spheres appear as white halos surrounding dark discs. The polymer matrix is visible in light grey.

As no major change was visible at F_L, the three views at F_{max} were selected. In the width and thickness views, the yellow rectangles indicate the areas where several coalesced decohesion caps appeared. A magnified and detailed view of these areas will be proposed later. The maximum decohesion caps appeared ahead of the right notch root, at least, on this cut. In the thickness view, the cluster of caps was rather located in the central part (yellow rectangle). It is no straightforward

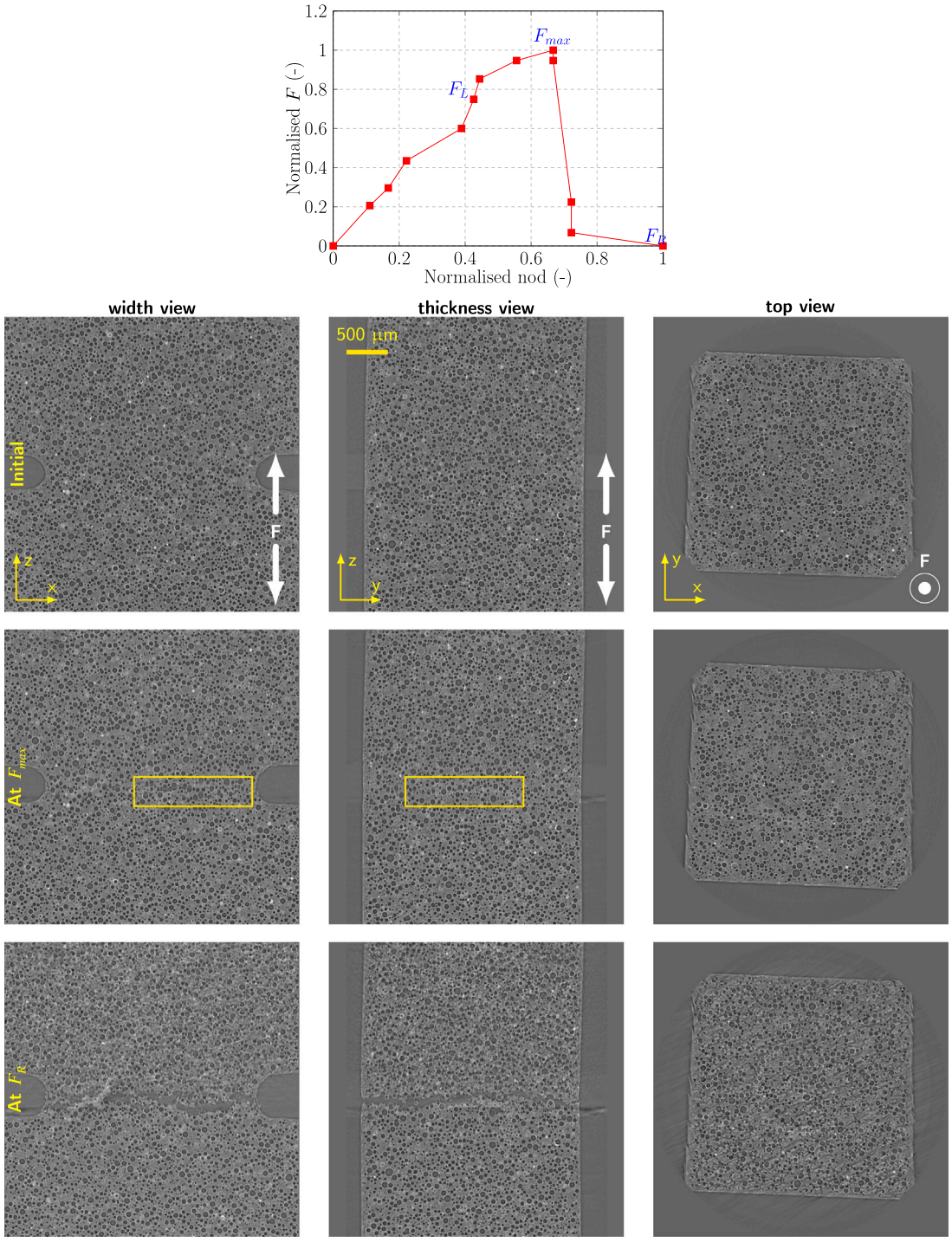

Fig. 15. Mechanisms of decohesion in the GSPP $N_{0.15}$ specimen.

to identify these coalesced caps in the top view, probably due to the non flatness of the surface.

At F_R, the crack is clearly identified although thinner than that of N_4. It probably initiated at mid-thickness and at a small distance ahead of the notch root. and propagated to the centre. This direction of crack propagation is completely different from N_4. No microsphere break was noticed in the whole data sets.

3.3.3. Mechanisms of decohesion at the scale of the microspheres

Fig. 16 details the mechanisms of the decohesion at the scale of the microspheres, on GSPP N_4 and $N_{0.15}$ specimens. The initiation of this phenomenon being at F_{max}, this moment was selected to focus on the areas where the maximum coalescence of decohesion was located depending on the notch root radius. Width and top views are respectively shown at the top and at the bottom of Fig. 16. The slices correspond to the views at mid-thickness (side views) and at the minimum cross section (top views). Red-dashed lines are used to identify the localisation of coalesced matrix-HGM decohesion. The north/south poles decohesion were concentrated at the notch, at mid-height, in both geometries. However, it was located at the specimen core in N_4 geometry whereas, in $N_{0.15}$ specimen, it is located near to the notch.

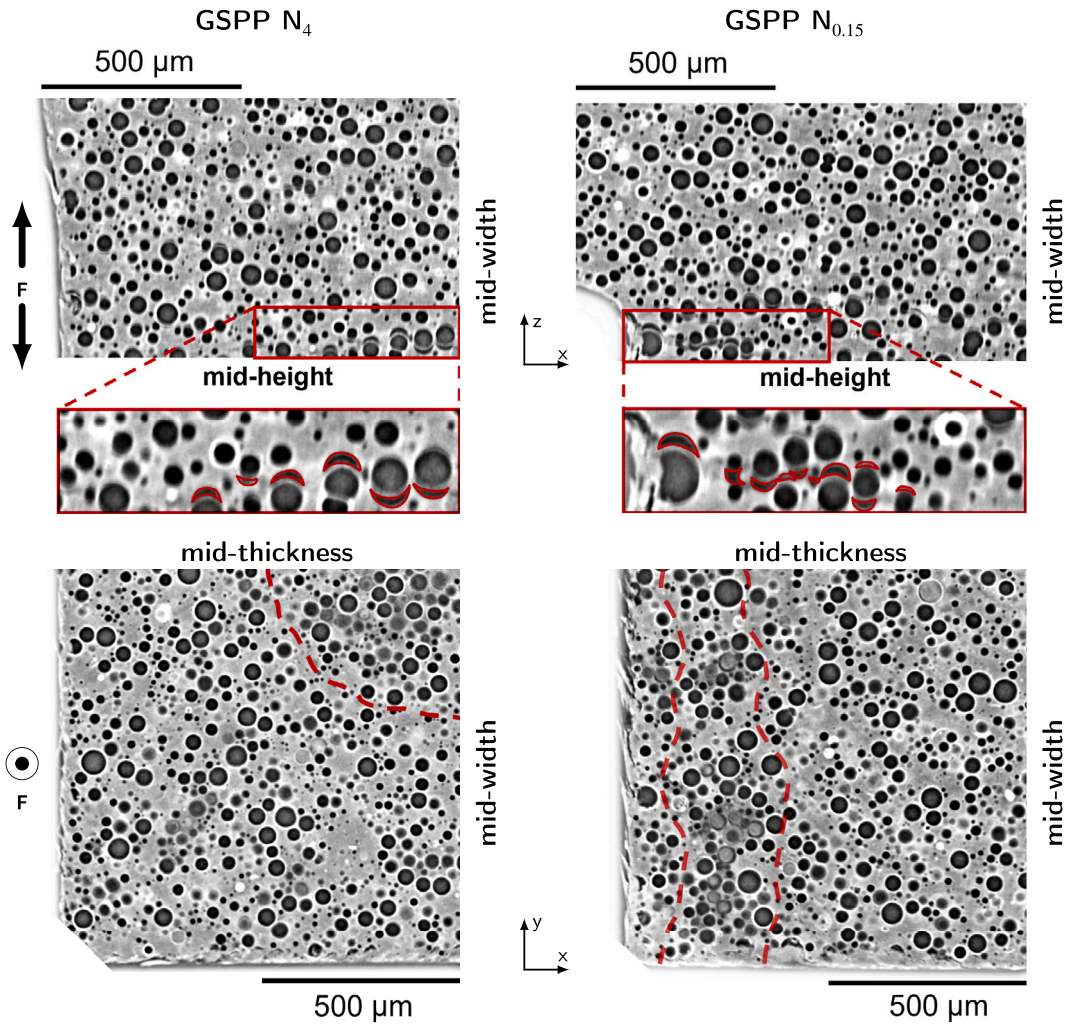

Fig. 16. Matrix-GSM decohesion at F_{max}. Side (top) and top views (bottom) of N_4 and$N_{0.15}$ specimens.

From the top view, a concentric distribution of the decohesion, grey halos, was noticed in the N_4 specimen. Besides, in $N_{0.15}$, decohesion was concentrated at 250 µm from the notch root. The proximity of the end of the caps promotes the coalescence of the decohesion, leading to the formation of a main crack. It can then be concluded that the initiation of the brittle crack in the GSPP is mainly due to the matrix-HGM decohesion followed by the coalescence of near neighbouring caps.

4. Conclusions

Glass Syntactic Polypropylene was investigated by *in situ* microtomography to better understand both the void nucleation and failure mechanisms during tensile loading.

Flat-notched geometries were cut-out from neat and Glass Syntactic Polypropylene extruded moulded plates. Notched specimens with two notch root radii, 4 mm and 0.15 mm named respectively N_4 and $N_{0.15}$, to set initial triaxial stress state in the minimum cross section, were used. Tensile tests and *in-situ* tensile tests were respectively carried-out at the laboratory and at the SOLEIL synchrotron radiation facilities.

Tomographic data sets, with a resolution of 1.3 µm, from stepwise tensile loading were retrieved from the notched zone. The tomographic data sets allowed gathering both the width and thickness evolution in the minimum cross section, and the notch opening displacement (nod) during the tests. The syntactic composite was studied following an inductive approach, *i.e.* from the resin — neat Polypropyle (PP), through isolated fillers — Single Hollow Glass Microsphere (SHGM), up to the syntactic foam — Glass Syntactic PolyPropylene (GSPP).

In line with literature, neat PP showed crazes concentration at the specimen notched volume, at mid-height, in both geometries. In the N_4 specimen, crazes were located at the geometry core, whereas, in the $N_{0.15}$ specimen, they were located at the notch root.

Interaction between crazes and decohesion of SHGM poles – decohesion caps – was noticed in resin-embedded isolated fillers. This latter being dependent on the opening stress, *i.e.* on the location of the considered point in a notched specimen, subjected to triaxial and heterogeneous stresses. Coalescence between crazes and decohesion caps was observed during tensile loading.

In GSPP, decohesion and rapid coalescence, due to the proximity of the microspheres (30% of volume ratio), were the leading failure mechanisms. Depending on the location of maximum craze and decohesion, the coalescence forms a main crack leading to the failure of the whole specimen. Once the main crack is initiated, the direction of propagation appears to differ: (i) from the centre to the free surface, through width and through thickness, for N_4; and (ii) from a small distance ahead of the notch to the centre for $N_{0.15}$. The results are in line with observed fractured surface morphology, from the tensile tests at the scale of the laboratory, where the mechanisms of void nucleation were highlighted *a posteriori*.

Although tomographic data sets were studied solely in a qualitatively way, these results have allowed a better understanding of the failure mechanisms of GSPP during multiaxial loading. The results

contribute to promote fostering innovation in the use of syntactic foams for fuel-efficient transport.

Future work should include the quantification of the crazing-related voids and decohesion caps; however, simultaneous surface and volume studies, DIC and Digital Volume Correlation (DVC), would be necessary to understand the effects of voids on the deformation distribution. In addition, the study of the failure mechanisms during compression loading should improve the understanding of the mechanical response of the GSPP under multiaxial loading.

CRediT authorship contribution statement

Theophile Hourdou: Methodology, Investigation, Formal analysis, Data curation. **Cristian Ovalle:** Writing – review & editing, Writing – original draft, Formal analysis, Conceptualization. **Sebastien Blassiau:** Supervision, Project administration, Funding acquisition. **Alain Thionnet:** Supervision, Project administration, Funding acquisition, Conceptualization. **Lucien Laiarinandrasana:** Writing – review & editing, Supervision, Project administration, Funding acquisition, Conceptualization.

Declaration of competing interest

The authors declare that they have no known competing financial interests or personal relationships that could have appeared to influence the work reported in this paper.

Data availability

Data will be made available on request.

References

[1] Malloy R, Hudson J. Foamed composites. In: International Encyclopedia of Composites, vol. 2, New York: VCH Publishers; 1990, p. 257–67.

[2] Bunn P, Mottram J. Manufacture and compression properties of syntactic foams. Composites 1993;24(7):565–71. http://dx.doi.org/10.1016/0010-4361(93)90270-I, URL https://www.sciencedirect.com/science/article/pii/001043619390270I.

[3] Wang L, Yang X, Zhang J, Zhang C, He L. The compressive properties of expandable microspheres/epoxy foams. Composites B 2014;56:724–32. http://dx.doi.org/10.1016/j.compositesb.2013.09.030, URL https://www.sciencedirect.com/science/article/pii/S135983681300543X.

[4] Zhang X, Wang P, Zhou Y, Li X, Yang E-H, Yu T, et al. The effect of strain rate and filler volume fraction on the mechanical properties of hollow glass microsphere modified polymer. Composites B 2016;101:53–63. http://dx.doi.org/10.1016/j.compositesb.2016.06.079, URL https://www.sciencedirect.com/science/article/pii/S1359836816311799.

[5] Yousaf Z, Smith M, Potluri P, Parnell W. Compression properties of polymeric syntactic foam composites under cyclic loading. Composites B 2020;186:107764. http://dx.doi.org/10.1016/j.compositesb.2020.107764, URL https://www.sciencedirect.com/science/article/pii/S1359836819306754.

[6] d'Almeida J. An analysis of the effect of the diameters of glass microspheres on the mechanical behavior of glass-microsphere/epoxy-matrix composites. Compos Sci Technol 1999;59(14):2087–91. http://dx.doi.org/10.1016/S0266-3538(99)00066-4, URL https://www.sciencedirect.com/science/article/pii/S0266353899000664.

[7] Gupta N, Zeltmann SE, Shunmugasamy VC, Pinisetty D. Applications of polymer matrix syntactic foams. JOM 2014;66:245–54. http://dx.doi.org/10.1007/s11837-013-0796-8.

[8] Zhu B, Zheng H, Wang J, Ma J, Wu J, Wu R. Tailoring of thermal and dielectric properties of LDPE-matrix composites by the volume fraction, density, and surface modification of hollow glass microsphere filler. Composites B 2014;58:91–102. http://dx.doi.org/10.1016/j.compositesb.2013.10.029, URL https://www.sciencedirect.com/science/article/pii/S1359836813006045.

[9] Saha M, Mahfuz H, Chakravarty U, Uddin M, Kabir ME, Jeelani S. Effect of density, microstructure, and strain rate on compression behavior of polymeric foams. Mater Sci Eng A 2005;406(1):328–36. http://dx.doi.org/10.1016/j.msea.2005.07.006, URL https://www.sciencedirect.com/science/article/pii/S0921509305006830.

[10] Wouterson EM, Boey FY, Hu X, Wong S-C. Specific properties and fracture toughness of syntactic foam: Effect of foam microstructures. Compos Sci Technol 2005;65(11):1840–50. http://dx.doi.org/10.1016/j.compscitech.2005.03.012, URL https://www.sciencedirect.com/science/article/pii/S0266353805000837.

[11] Gupta N, Nagorny R. Tensile properties of glass microballoon-epoxy resin syntactic foams. J Appl Polym Sci 2006;102(2):1254–61. http://dx.doi.org/10.1002/app.23548, arXiv:https://onlinelibrary.wiley.com/doi/pdf/10.1002/app.23548, URL https://onlinelibrary.wiley.com/doi/abs/10.1002/app.23548.

[12] Gupta N, Ye R, Porfiri M. Comparison of tensile and compressive characteristics of vinyl ester/glass microballoon syntactic foams. Composites B 2010;41(3):236–45. http://dx.doi.org/10.1016/j.compositesb.2009.07.004, URL https://www.sciencedirect.com/science/article/pii/S135983680900153X.

[13] Kumar BB, Doddamani M, Zeltmann SE, Gupta N, Ramakrishna S. Data characterizing tensile behavior of cenosphere/HDPE syntactic foam. Data Brief 2016;6:933–41. http://dx.doi.org/10.1016/j.dib.2016.01.058, URL https://www.sciencedirect.com/science/article/pii/S2352340916300105.

[14] Yousaf Z, Morrison NF, Parnell WJ. Tensile properties of all-polymeric syntactic foam composites: Experimental characterization and mathematical modelling. Composites B 2022;231:109556. http://dx.doi.org/10.1016/j.compositesb.2021.109556, URL https://www.sciencedirect.com/science/article/pii/S1359836821009227.

[15] Tagliavia G, Porfiri M, Gupta N. Analysis of flexural properties of hollow-particle filled composites. Composites B 2010;41(1):86–93. http://dx.doi.org/10.1016/j.compositesb.2009.03.004, URL https://www.sciencedirect.com/science/article/pii/S1359836809000390.

[16] Adrien J, Maire E, Gimenez N, Sauvant-Moynot V. Experimental study of the compression behaviour of syntactic foams by in situ X-ray tomography. Acta Mater 2007;55(5):1667–79. http://dx.doi.org/10.1016/j.actamat.2006.10.027, URL https://www.sciencedirect.com/science/article/pii/S135964540600752X.

[17] Lachambre J, Maire E, Adrien J, Choqueuse D. In situ observation of syntactic foams under hydrostatic pressure using X-ray tomography. Acta Mater 2013;61(11):4035–43. http://dx.doi.org/10.1016/j.actamat.2013.03.017, URL https://www.sciencedirect.com/science/article/pii/S1359645413002279.

[18] Huang R, Li P, Wang Z, Liu T. X-Ray microtomographic characterization and quantification of the strain rate dependent failure mechanism in cenosphere epoxy syntactic foams. Adv Energy Mater 2016;18(9):1550–5. http://dx.doi.org/10.1002/adem.201600215, arXiv:https://onlinelibrary.wiley.com/doi/pdf/10.1002/adem.201600215, URL https://onlinelibrary.wiley.com/doi/abs/10.1002/adem.201600215.

[19] Croom BP, Jin H, Mills B, Carroll J, Long K, Brown J, et al. Damage mechanisms in elastomeric foam composites: Multiscale X-ray computed tomography and finite element analyses. Compos Sci Technol 2019;169:195–202. http://dx.doi.org/10.1016/j.compscitech.2018.11.025, URL https://www.sciencedirect.com/science/article/pii/S0266353818319262.

[20] Croom BP, Jin H, Carroll J, Long K, Li X. Particle clustering effects on damage mechanisms in elastomeric syntactic foams. Composites B 2019;175:107160. http://dx.doi.org/10.1016/j.compositesb.2019.107160, URL https://www.sciencedirect.com/science/article/pii/S1359836818338794.

[21] ISO. Plastics — Determination of tensile properties — Part 2: Test conditions for moulding and extrusion plastics. 2012.

[22] Boisot G, Laiarinandrasana L, Besson J, Fond C, Hochstetter G. Experimental investigations and modeling of volume change induced by void growth in polyamide 11. Int J Solids Struct 2011;48(19):2642–54. http://dx.doi.org/10.1016/j.ijsolstr.2011.05.016, URL https://www.sciencedirect.com/science/article/pii/S0020768311001880.

[23] Paganin D, Mayo SC, Gureyev TE, Miller PR, Wilkins SW. Simultaneous phase and amplitude extraction from a single defocused image of a homogeneous object. J Microsc 2002;206(1):33–40. http://dx.doi.org/10.1046/j.1365-2818.2002.01010.x, arXiv:https://onlinelibrary.wiley.com/doi/pdf/10.1046/j.1365-2818.2002.01010.x, URL https://onlinelibrary.wiley.com/doi/abs/10.1046/j.1365-2818.2002.01010.x.

[24] Mirone A, Brun E, Gouillart E, Tafforeau P, Kieffer J. The PyHST2 hybrid distributed code for high speed tomographic reconstruction with iterative reconstruction and a priori knowledge capabilities. Nucl Instrum Methods Phys Res B 2014;324:41–8. http://dx.doi.org/10.1016/j.nimb.2013.09.030, URL https://www.sciencedirect.com/science/article/pii/S0168583X14000251, 1st International Conference on Tomography of Materials and Structures.

[25] Pelerin M, King A, Laiarinandrasana L, Proudhon H. Development of a versatile mechanical testing device for in situ synchrotron tomography and diffraction experiments. Integrating Mater Manuf Innov 2019;8(1):378–87. http://dx.doi.org/10.1007/s40192-019-00143-6.

[26] Proudhon H, Pelerin M, King A, Ludwig W. In situ 4D mechanical testing of structural materials: The data challenge. Curr Opin Solid State Mater Sci 2020;24(4):100834. http://dx.doi.org/10.1016/j.cossms.2020.100834, URL https://www.sciencedirect.com/science/article/pii/S1359028620300322.

[27] Ovalle C, Boisot G, Laiarinandrasana L. Effects of stress triaxiality ratio on the heat build-up of polyamide 11 under loading. Mech Mater 2020;145:103375. http://dx.doi.org/10.1016/j.mechmat.2020.103375, URL https://www.sciencedirect.com/science/article/pii/S0167663619306167.

[28] Schindelin J, Arganda-Carreras I, Frise E, Kaynig V, Longair M, Pietzsch T, et al. Fiji: An open-source platform for biological-image analysis. Nature Methods 2012;9:676–82.

[29] ThermoFisher Scientific. Avizo software. 2020, URL https://www.thermofisher.com/fr/fr/home/electron-microscopy/products/software-em-3d-vis/avizo-software.html.

[30] Laiarinandrasana L, Klinkova O, Nguyen F, Proudhon H, Morgeneyer TF, Ludwig W. Three dimensional quantification of anisotropic void evolution in deformed semi-crystalline polyamide 6. Int J Plast 2016;83:19–36. http://dx.doi.org/10.1016/j.ijplas.2016.04.001, URL https://www.sciencedirect.com/science/article/pii/S0749641916300444.

[31] Laiarinandrasana L, Selles N, Klinkova O, Morgeneyer TF, Proudhon H, Helfen L. Structural versus microstructural evolution of semi-crystalline polymers during necking under tension: Influence of the skin-core effects, the relative humidity and the strain rate. Polym Test 2016;55:297–309. http://dx.doi.org/10.1016/j.polymertesting.2016.09.012, URL https://hal.archives-ouvertes.fr/hal-01717685.

[32] Selles N, King A, Proudhon H, Saintier N, Laiarinandrasana L. Time dependent voiding mechanisms in polyamide 6 submitted to high stress triaxiality: experimental characterisation and finite element modelling. Mech Time-Dependent Mater 2018;22(3):351–71. http://dx.doi.org/10.1007/s11043-017-9360-1.

[33] Rojek J, Breite C, Swolfs Y, Laiarinandrasana L. Void growth measurement and modelling in a thermosetting epoxy resin using SEM and tomography techniques. Contin Mech Thermodyn 2020;32(2):471–88. http://dx.doi.org/10.1007/s00161-020-00865-5.

[34] Bridgman P. The stress distribution at the neck of a tension specimen. Trans ASM 1944;32:553–74.

[35] Bridgman P. The effect of nonuniformities of stress at the neck of a tension specimen. In: Studies in large plastic flow and fracture with special emphasis on the effects of hydrostatic pressure. McGraw-Hill; 1952, p. 9–37.

[36] Ognedal AS, Clausen AH, Dahlen A, Hopperstad OS. Behavior of PVC and HDPE under highly triaxial stress states: An experimental and numerical study. Mech Mater 2014;72:94–108. http://dx.doi.org/10.1016/j.mechmat.2014.02.002, URL https://www.sciencedirect.com/science/article/pii/S0167663614000234.

[37] Laiarinandrasana L, Morgeneyer T, Proudhon H, N'guyen F, Maire E. Effect of multiaxial stress state on morphology and spatial distribution of voids in deformed semicrystalline polymer assessed by X-ray tomography. Macromolecules 2012;45:4658–68. http://dx.doi.org/10.1021/ma3005247.

[38] Cheng Y, Laiarinandrasana L, Helfen L, Proudhon H, Klinkova O, Baumbach T, et al. 3D damage micromechanisms in polyamide 6 ahead of a severe notch studied by in situ synchrotron laminography. Macromol Chem Phys 2016;217(5):701–15. http://dx.doi.org/10.1002/macp.201500316, arXiv:https://onlinelibrary.wiley.com/doi/pdf/10.1002/macp.201500316, URL https://onlinelibrary.wiley.com/doi/abs/10.1002/macp.201500316.

[39] Ovalle C, Cloetens P, Proudhon H, Morgeneyer TF, Laiarinandrasana L. Nanocavitation mechanisms in deformed high density PolyEthylene (HDPE) using synchrotron radiation NanoTomography. Polymer 2021;229:123959. http://dx.doi.org/10.1016/j.polymer.2021.123959, URL https://www.sciencedirect.com/science/article/pii/S0032386121005826.

[40] Morgeneyer TF, Proudhon H, Cloetens P, Ludwig W, Roirand Q, Laiarinandrasana L, et al. Nanovoid morphology and distribution in deformed HDPE studied by magnified synchrotron radiation holotomography. Polymer 2014;55(25):6439–43. http://dx.doi.org/10.1016/j.polymer.2014.10.022, URL https://www.sciencedirect.com/science/article/pii/S0032386114009203.